Available online at www.sciencedirect.com
ScienceDirect
Acta Materialia 54 (2006) 4621–4631
Acta MATERIALIA
www.actamat-journals.com

Precipitation kinetics and transformation of metastable phases in Al–Mg–Si alloys

C.-S. Tsao [a,*], C.-Y. Chen [a], U.-S. Jeng [b], T.-Y. Kuo [c]

[a] Nuclear Fuel and Materials Division, Institute of Nuclear Energy Research, P.O. Box 3-14, 1000 Wenhua Road, Longtan, Taoyuan 32546, Taiwan
[b] National Synchrotron Radiation Research Center, Hsinchu 30076, Taiwan
[c] Department of Mechanical Engineering, Southern Taiwan University of Technology, 71005, Taiwan

Received 21 November 2005; received in revised form 1 June 2006; accepted 1 June 2006
Available online 28 August 2006

Abstract

In situ synchrotron small-angle X-ray scattering (SAXS) and transmission electronic microscopy were used to study the precipitation and transformation behaviors of metastable β″ and β′ phases of naturally aged Al–Mg–Si alloys, AA 6022, during continuous heating, and subsequent isothermal aging. A new SAXS analysis approach for the complex SAXS profiles enabled a quantitative analysis of the structural evolution and the corresponding kinetics of the concurrent needle-like β″ and rod-like β′ phase transformations, of different size characteristics. The stable cross-section and rapid length growth along the needles of β″ phase, and the radius growth of β′ phase during the temporal evolution were characterized well by the concomitant nucleation, growth and coarsening stages. For an alloy aged at 260 °C, the β″ precipitates (∼3.5 nm in radius) and β′ precipitates (∼10.5 nm in radius) reached the coarsening stages at $t = 30$ and 210 min, respectively. During the coarsening stage, the β″ precipitates dissolved partially into the matrix and transformed partially to the β′ phase, and then stabilized with the residual ∼65% precipitates. The same methodology was also applied to an Al–Mg–Si alloy, AA 6111, containing Cu. The β″ precipitates of AA 6111 alloy aged at 180 °C showed an inert radius (∼1.8 nm) and a growing length with aging time, and the longer incubation period of ∼60 min observed in the early stage of precipitation, relative to AA 6022, was attributed to the more natural clusters.
© 2006 Acta Materialia Inc. Published by Elsevier Ltd. All rights reserved.

Keywords: Small-angle X-ray scattering; Aluminum alloys; Precipitation; Aging

1. Introduction

Al–Mg–Si alloys are much used in the aerospace and automotive industries, owing to the combined merits of low weight and good mechanical properties. The mechanical properties of the alloys are mainly attributed to the metastable precipitate phases formed during artificial aging. A generally accepted precipitation sequence of solution-treated Al–Mg–Si alloys during artificial aging is: α supersaturated solid solution (SSS) → GP-I zones → metastable needle-like β″ precipitates (or called GP-II zones; formed through the transformation of GP-I as nuclei) → metastable rod-like (or lath-like) β′ precipitates → stable β phase. Numerous investigations [1–13] using transmission electronic microscopy (TEM) and differential scanning calorimetry (DSC) have been conducted for the characterizations of nanostructures and precipitation behavior of β″ precipitates in Al–Mg–Si alloys aged at ∼180 °C. Nevertheless, the understanding of β″ precipitation is still incomplete and limited. Most studies [14–19] of the nanoscaled β′ and β″ phases formed during higher-temperature aging have focused only on the qualitatively complex precipitation sequence and crystal structures.

Recently, small-angle X-ray and neutron scattering (SAXS and SANS), being effective tools for in situ studies of particles' nanostructural evolution in a bulk sample, have attracted certain attention [20–23]. However, the

* Corresponding author.
E-mail address: cstsao@iner.gov.tw (C.-S. Tsao).

1359-6454/$30.00 © 2006 Acta Materialia Inc. Published by Elsevier Ltd. All rights reserved.
doi:10.1016/j.actamat.2006.06.005

application of SANS to the study of Al–Mg–Si alloy is still in an early stage, and provides only limited data [7] and rough analysis [24] of β″ precipitates. Because the SAXS contrast between the precipitates (MgSi) and the Al matrix is very low, our previous SAXS study [25] using high-energy photons from a high-flux synchrotron radiation source and the established analysis technique constitutes the first SAXS report on the temporal evolution of β″ precipitate structure in an AA 6022 Al–Mg–Si alloy, including radius, length and volume fraction.

In the present study, using the in situ synchrotron SAXS technique, the time-dependent SAXS profiles measured can be characterized by two regimes: the $Q > 0.04$ Å^{-1} regime contributed by needle-like β″ precipitates of a typical radius of ~3 nm and the $Q < 0.04$ Å^{-1} regime dominated by rod-like β′ precipitates of a typical radius of ~10 nm. Due to the substantial difference in size, the two scattering contributions by β″ and β′ precipitates can be separated relatively well from the SAXS profiles for a quantitative investigation of the kinetics of the two concurrent β″ and β′ transformations, each having its own process of precipitation and dissolution, during artificial aging. The in situ SAXS result provides a basis for improving the current understanding of the transformation behaviors of the metastable phases in Al–Mg–Si alloys.

Generally, studies of Al–Mg–Si alloys focus on two aging temperatures: ~180 °C for β″ precipitates and ~260 °C for β′ as well as β″ precipitates. In addition to the typical Al–Mg–Si ternary alloys (e.g., AA 6022 alloy), Al–Mg–Si alloys containing Cu (quaternary alloys, e.g., AA 6111 alloy) have also attracted much interests in industrial research [6,11]. Study of both AA 6022 and AA 6111 aged at ~180 °C centers mainly on the comparison of precipitate types [5]. In the study reported here, we performed in situ SAXS for both AA 6022 and AA 6111 Al–Mg–Si alloys. We investigated the time-resolved nanostructural evolutions of β″ and β′ precipitates in AA 6022 alloy during a continuous heating process from room temperature (RT) and the subsequent isothermal aging at 260 °C; the natural aging effect at RT was also included [1,9,10,26]. The corresponding precipitation and dissolution kinetics of the concurrent β″ and β′ phase transformations are quantitatively established. The temporal evolutions of the precipitate size and volume fraction in the precipitation process for each metastable phase can be well characterized by the concomitant nucleation, growth and coarsening stages proposed in the classic theory [27] and numerical modeling [28–31]. A comparison of structural evolutions of the β″ precipitates with aging time in AA 6022 and AA 6111 alloys aged at 180 °C is also presented. TEM observations of the same AA 6022 and AA 6111 alloy specimens studied by SAXS complement and confirm the SAXS analysis.

2. Experimental

Al–Mg–Si alloys AA 6022 and AA 6111 were received from Alcoa Inc., USA, in the form of ~1 mm thick sheets. The as-received sheets had been homogenized, hot rolled, cold rolled and then commercially heat-treated with the temper designations of 6022-T4E29 and 6111-T43. The fine grains serving as the matrix do not contribute to the SAXS profile because of no scattering contrast effect. The composition (wt.%) of the alloys in this study were: 0.58 Mg, 1.15 Si, 0.13 Fe, 0.06 Cu and 0.06 Mn for AA 6022 alloy; and 0.75 Mg, 0.9 Si, 0.4 Fe, 0.7 Cu and 0.3 Mn for AA 6111 alloy.

Before SAXS measurements, the sample sheets were solution-treated at 560 °C for 40 min, and subsequently quenched into ice water. Quenched samples were naturally aged for 30 days at RT. The SAXS specimens were prepared into 1 cm × 1 cm area and an optimum thickness of 0.5 mm by cutting the sheets and grinding. These specimens, fixed inside a small furnace with air-circulation cooling, were then heat-treated for combination with in situ SAXS measurements. The heat treatments of the SAXS specimens are listed in Table 1. The SAXS measurements were conducted using the SAXS setup at the BL01B beamline of the National Synchrotron Radiation Research Center (NSRRC), Taiwan. The experimental details and advantages of in situ SAXS using the high-energy, high-flux synchrotron radiation X-ray source were described in our previous SAXS study [25]. The in situ SAXS data were collected during a heating process from RT and the subsequent isothermal aging. During the isothermal aging, typical SAXS data were collected continuously on the basis of each frame/30 min. The standard deviation of the SAXS data collected during the isothermal aging was typically within ±2% due to the 30 min counting interval and the high intensity, while the standard deviation of the SAXS profiles collected during the heating process (usually 5 min counting interval) was within ±20%. The standard deviations (shown as error bars in some of the figures presented) decrease significantly with the increase of the SAXS intensities. In general, the high-Q SAXS data at low heating temperatures have larger error bars. All the SAXS scattering profiles $I(Q)$ were measured in an absolute scattering scale [25], with the scattering vector $Q = 4\pi\sin(\theta/2)/\lambda$ defined by the scattering angle θ and the X-ray wavelength λ.

The use of 15 keV synchrotron photons here cannot enhance any nucleation or precipitation. The radiation-induced or radiation-enhanced precipitation is caused by

Table 1
Heat treatments of the specimens conducted for SAXS measurements

Alloy type	Heat treatment
AA 6022	Continuous heating process from RT to 260 °C with a rate 5 °C/min, then followed by isothermal aging at 260 °C for 720 min
AA 6111	Continuous heating process from RT to 180 °C with a rate 5 °C/min, then followed by isothermal aging at 180 °C for 400 min

striking atoms out of the lattice sites, thus creating vacancies. The condition for attaining such effects [32] requires massive and energetic particles of at least hundreds of keV, whereas the photon energy used for SAXS is only 15 keV.

TEM examination was performed using a JEM 2000FX at 200 kV. The TEM specimens were prepared by cutting a small piece from the samples, mechanically grinding to 60–80 μm thickness and then jet polishing in a solution of 30 vol.% HNO_3 and 70 vol.% CH_3OH at −20 °C. Diffraction contrast was applied to image the particle size. The TEM observations were conducted for both the AA 6022 and AA 6111 samples without and with the aging treatments used for the SAXS measurements.

3. Results and discussion

3.1. Structural evolution and precipitation kinetics of β″ and β′ phases during continuous heating

The time-dependent SAXS profiles measured for the naturally aged AA 6022 alloy during the heating process from RT to 260 °C are selectively presented in Fig. 1(a), together with that for the subsequent isothermal artificial aging at 260 °C for 30 min. Note that the SAXS profile obtained for isothermal aging at 260 °C is of an intensity four times higher than that observed for the same sample aged at 180 °C [25], which is consistent with the reported SANS data [24]. The SAXS profiles measured during continuous heating from RT to 211 °C were nearly the same, indicating no observable structural change. During the heating from RT to 211 °C, the power law scattering of Q^{-4} in the low-Q region corresponds to the asymptotic scattering behavior of other large particles. This type of large particles are constituent or segregated particles from the Fe and Mn impurities. Their estimated size is at least close to the scale of micrometers. The SAXS intensity in the intermediate-Q region can be attributed to the scattering from the clusters formed during natural aging. These natural aging clusters were also confirmed by our TEM work. The observed natural aging clusters are spherical particles of roughly 2–5 nm in diameter. The cut-off image detection limit using the diffraction contrast here is ~1.5 nm for the crystalline specimens.

During heating from 211 to 260 °C, the SAXS profile intensities increase with temperature in the intermediate- to high-Q region ($Q \geqslant 0.05$ Å^{-1}), indicating a nucleation and growth of β″ precipitates. (Note that this Q region is almost entirely contributed by the scattering of β″ precipitates as mentioned in Section 1.) In contrast, the corresponding heat flow due to the formation of β″ precipitates was observed at 240–260 °C in previous DSC studies [1,2,6,11]. The SAXS profiles collected for the range 235–260 °C and the subsequent isothermal aging at 260 °C for 30 min are nearly the same in the intermediate- to high-Q region, implying the development of β″ precipitates enters a coarsening stage (i.e., no change in volume fraction according to the well-known LSW theory [27]).

Above 235 °C, the SAXS profile intensity in the low-Q region, dominated by newly formed large precipitates, increases with temperature and aging time, and changes gradually from the behavior of $I(Q) \propto Q^{-4}$ (at RT) to $I(Q) \propto Q^{-2.1}$. The Q^{-4} dependence in the low-Q region is

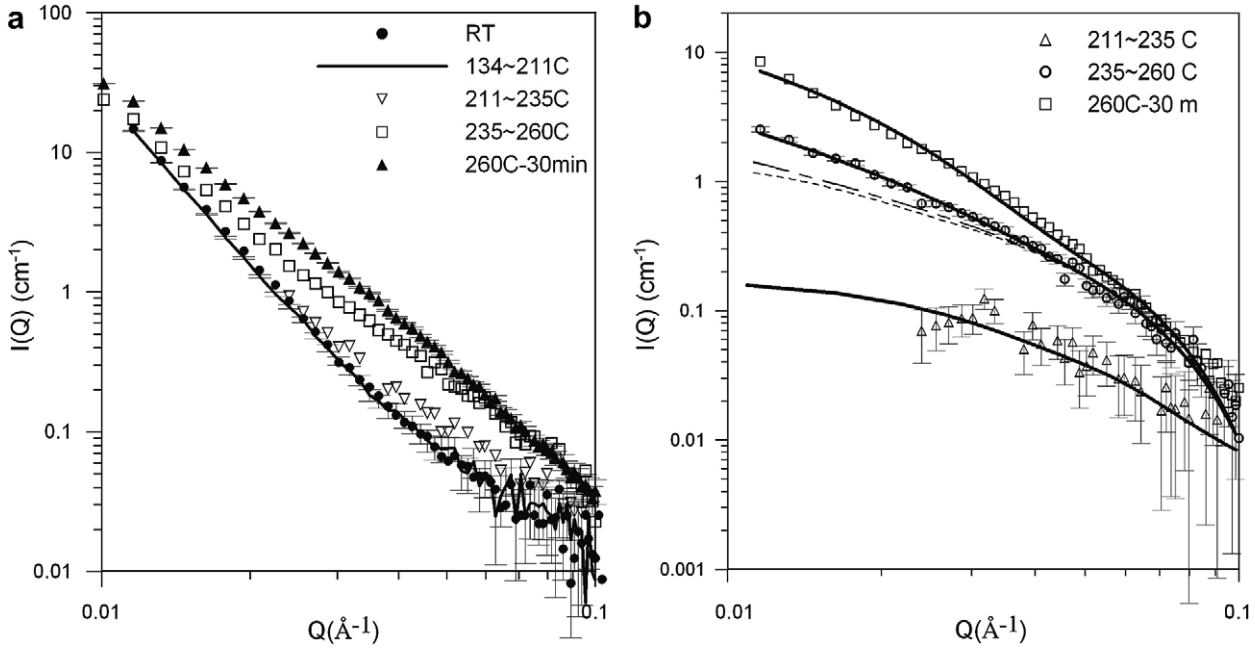

Fig. 1. (a) Selected time-dependent SAXS profiles measured for the naturally aged alloy AA6022 during continuous heating from RT to 260 °C, together with that obtained during subsequent isothermal artificial aging at 260 °C for 30 min. (b) The SAXS profile obtained at RT is subtracted from the measured SAXS profiles corresponding to (a) to remove the contribution of natural aging clusters. The solid lines are the intensities calculated from the model fittings. (The abscissa is scattering vector Q. The ordinate is SAXS intensity expressed by macroscopic cross-section per sample volume.)

attributed to the additional large particles formed at RT, which do not vary with aging time and the heating process, as explained in Section 3.3 below and in a previous study [25]. The transition of the scattering characteristics is mainly due to the nucleation and growth of the rod-like β′ precipitates of a much larger size than the β″ precipitates formed concurrently. The large β′ precipitates were confirmed as the main precipitates during aging at 260 °C in many previous TEM studies [15–18]. These TEM studies also reported that the needle-like β″ precipitates coexist with the rod-like (or lath-like) β′ precipitates in the initial period of aging.

To remove the scattering contributions from the natural aging clusters and other large particles existing prior to the heating process, the time-resolved SAXS profiles shown in Fig. 1(a) are processed by subtracting the SAXS profile measured at RT. The resulting SAXS profiles shown in Fig. 1(b) are mainly attributed to the contributions from the β″ and β′ precipitates [24,25]. Here, we have used the assumption that the natural aging clusters and other large particles are inert during the heating process and the subsequent isothermal aging. This assumption neglects the small fraction of natural aging clusters which indeed dissolved during the heating and/or the artificial aging, and result in a slightly over-subtraction effect. Nevertheless, the over-subtraction effect is increasingly smaller for the SAXS profiles measured at later times, where the β″ and β′ precipitates contribute more and more. Therefore, during heating at 211–235 °C, the β′ precipitates being supposed insignificant, we model the corrected SAXS intensity from the β″ precipitates formed during heating at 211–235 °C with thin cylindrical particles:

$$I_{\beta''}(Q) = \eta(\Delta\rho)^2 V_{\mathrm{P}} \tilde{P}(Q) + B \tag{1}$$

where the contrast $\Delta\rho$ is the scattering length density difference between precipitates and matrix, η is the volume fraction of β″ precipitates, V_{P} is the volume of the cylindrical particles of radius R and length L and B is the constant incoherent background contribution. The normalized form factor $\tilde{P}(Q)$ [20] for cylindrical particles, averaged in orientation, can be expressed as

$$\tilde{P}(Q) = \int_0^{\pi/2} \left(\frac{\sin\left(\frac{QL}{2}\cos\varphi\right)}{\frac{QL}{2}\cos\varphi} \right)^2 \left(\frac{2J_1(QR\sin\varphi)}{QR\sin\varphi} \right)^2 \sin\varphi \, \mathrm{d}\varphi \tag{2}$$

where J_1 is the first-order Bessel function. The radius and length extracted from the model fitting of Eq. (1) are 3.1 ± 1.0 nm and 18.3 ± 18 nm, respectively, which are consistent with those obtained from the previous SAXS analysis of β″ precipitates in AA 6022 alloy aged at 180 °C [21], and the TEM studies [1,2,5–7] reported previously. The uncertainties of the radius and length are the standard deviations obtained from a non-linear least-squares data fitting process (χ^2 optimization). The calculated SAXS profile using the structural parameters agrees well with the measured SAXS data, as shown in Fig. 1(b).

For the SAXS profiles collected above 235 °C, the scattering contribution from β′ precipitates is increasingly important as the aging time increases, and has to be taken into account together with that from the β″ precipitates. The scattering contribution from the β″ precipitates, dominating the intermediate- to high-Q region ($0.045 \leqslant Q \leqslant 0.1$ Å^{-1}) of the SAXS profiles (mentioned previously) can be approximated by

$$I(Q) \propto \frac{\pi}{QL} \exp(-R^2Q^2/4)$$

in the intermediate-Q region, $2\pi/L \leqslant Q \leqslant \pi/R$ (Kratky–Porod approximation) [21], according to Eqs. (1) and (2). Note that this scattering contribution is closely related to the radius of β″ precipitates. On the other hand, the scattering profile in the low-Q region, $0.01 \leqslant Q \leqslant 0.045$ Å^{-1}, is dominated mainly by the scattering profile of large β′ precipitates (where the profile relates closely to the radius of the rod-like β′ precipitates with a radius $R \geqslant 80$ Å). The scattering profile in the low-Q region contributed by the length of the β″ precipitates is a relatively slow-varying profile. As shown in Fig. 1(b), the calculated scattering profiles of needle-like β″ precipitates with the same $R = 3$ nm but $L = 50$ nm (dotted line), 200 nm and 300 nm (dashed lines) in the low-Q region do not vary much with the length. Therefore, the SAXS profiles in this low-Q region can be considered as the sum of the contributions mainly from the radius of larger β′ precipitates as well as the length of β″ precipitates. For the SAXS analysis presented below, we can extract the time-dependent structural parameters of the concurrent β″ and β′ precipitates at the same time by the method of model fitting.

Technically, the SAXS intensity from the needle-like β″ and rod-like β′ precipitates formed above ~235 °C can be approximated by extending Eq. (1) for β″ phase with the Kratky–Porod approximation for β′ phase as follows:

$$\begin{aligned} I(Q) &= N_{\beta'}(\Delta\rho_{\beta'})^2 \frac{V_{\beta'}\pi R_0^2}{Q} \exp(-R_0^2Q^2/4) \\ &\quad + \eta(\Delta\rho)^2 V_{\mathrm{P}} \tilde{P}(Q) + B \\ &= \eta_{\beta'}(\Delta\rho_{\beta'})^2 \frac{\pi R_0^2}{Q} \exp(-R_0^2Q^2/4) + \eta(\Delta\rho)^2 V_{\mathrm{P}} \tilde{P}(Q) + B \\ &= \frac{C\pi R_0^2}{Q} \exp(-R_0^2Q^2/4) + \eta(\Delta\rho)^2 V_{\mathrm{P}} \tilde{P}(Q) + B \end{aligned} \tag{3}$$

where the pre-factor C relates to the scattering contrast $\Delta\rho_{\beta'}$ and volume fraction $\eta_{\beta'}$ of the rod-like β′ precipitates, with radius R_0, particle volume $V_{\beta'}$ and number density $N_{\beta'}$. The precipitate composition usually remains a constant during the classical nucleation, growth and coarsening. Therefore, the pre-factor C can be regarded as a relative volume fraction index of the β′ phase.

Some TEM studies [15–17] pointed out that, in addition to β′ precipitates, some other types of metastable precipitates, denoted as β'_{A}, β'_{B} and β'_{C}, could coexist in the excess Si-type Al–Mg–Si alloy (e.g., the AA 6022 alloy used). Nevertheless, all these types of precipitates have

similar morphologies and sizes (lath-like or rod-like), except the crystal structures. The radius of the β′ precipitates observed by our TEM work (see Section 3.2) is consistent with the sizes observed by other TEM studies [15–17]. Therefore, the different types of β′ precipitates can all have similar SAXS profiles, but with different scattering contrasts (for different scattering intensities) arising from the different crystal structures. The SAXS intensity from all the types of β′ precipitates can be approximated in this study by a convoluted profile with an effective contrast.

The radii of β″ and β′ precipitates, R and R_0, extracted from the model fitting using Eq. (3) for SAXS data of the AA 6022 alloy collected during heating at 235–260 °C and the subsequent isothermal aging at 260 °C are summarized in Table 2. The model-fitted length of β″ precipitates increases largely during the heating process from 18.3 nm at 211–235 °C to 150 nm at 235–260 °C, and then shows a continuous growing trend during the aging at 260 °C. From the calculated scattering profiles (the dotted and dashed lines in Fig. 1(b)), the model-dependent fitting in the measured Q range may extrapolate a large length of 150 nm with a large uncertainty. The model-fitted values for β′ precipitates are also greater than 150 nm with a large uncertainty. The calculated SAXS profiles simulated well the measured SAXS data, as shown in Fig. 1(b). Note that the temporal evolution of the model-fitted values for the β″ precipitates reveals an inert radius and a rapid growing length with aging time. The temporal evolutions of the relative volume fractions obtained from the model fitting for β″ and β′ precipitates are shown in Fig. 2 (also see Table 2). The relative volume fraction of β′ precipitates is determined by the fitted pre-factor C values of the Kratky–Porod term in Eq. (3).

In the present study, the volume fraction for each phase is normalized by the maximum value during the continuous heating and the isothermal aging. The structural evolutions of β″ and β′ precipitates during the continuous heating in terms of size and volume fraction can be characterized by the early stage of a typical precipitation, i.e., the concomitant nucleation and growth [27–31]. From Fig. 2, this in situ SAXS measurement detects the β″ and β′ precipitations at a slightly earlier temperature than those observed by DSC [1,2,6,11] and TEM [17] measurements.

Table 2
Radii and relative volume fractions of β″ and β′ precipitates determined by the model fitting of SAXS data of the AA 6022 alloy obtained selectively during isothermal aging at 260 °C

Aging time (min)	β″ phase		β′ phase	
	R (nm)	Relative volume fraction	R_0 (nm)	Relative volume fraction
211–235 °C[a]	3.1 ± 32%	0.14 ± 61%		
235–260 °C[a]	3.1 ± 10%	0.80 ± 13%	9.0 ± 5%	0.08 ± 18%
30	3.1 ± 2%	1.00 ± 2%	9.1 ± 1%	0.44 ± 3%
90	3.2 ± 2%	0.83 ± 2%	9.5 ± 1%	0.77 ± 3%
150	3.4 ± 2%	0.82 ± 2%	10.1 ± 1%	0.83 ± 3%
210	3.5 ± 2%	0.79 ± 2%	10.5 ± 2%	1.00 ± 5%
360	3.5 ± 2%	0.73 ± 3%	10.5 ± 2%	1.00 ± 5%
510	3.4 ± 2%	0.65 ± 3%	10.5 ± 2%	1.00 ± 5%

[a] During continuous heating from RT to 260 °C.

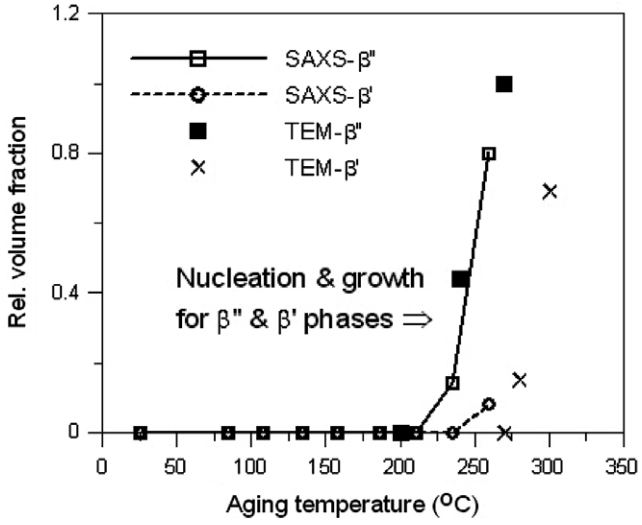

Fig. 2. Comparison of the temporal evolutions of relative volume fractions of β″ and β′ precipitates obtained from the SAXS model fitting and TEM observations [17] during continuous heating for AA 6022 alloy. (The volume fraction for each phase is normalized by the maximum value during continuous heating and isothermal aging.)

3.2. Phase transformation kinetics of β″ concurrent with β′ phases during isothermal aging at 260 °C

The time-dependent SAXS profiles measured during isothermal artificial aging at 260 °C (up to 210 min) are fitted using the same Eq. (3) for the time-dependent structural parameters of the β″ and β′ precipitates in the isothermal aging. The fitted data are selectively presented in Fig. 3(a). We have also carried out model-independent Kratky–Porod approximations (solid lines in Fig. 3(b)) in the different Q regions corresponding to the β″ and β′ regimes for the representative SAXS profiles collected during the artificial aging. The radii extracted from the approximation (the slopes of the fitted lines in the $\ln(I(Q)\cdot Q)$ vs. Q^2 plot) for the β′ and β″ precipitates, ensuring the increasing trend of the radii with aging time, are consistent with those obtained from the model fitting of Eq. (3). Note that the observed in situ SAXS profiles with a crossover at $\sim 0.04\ \text{Å}^{-1}$ also show the different temporal behaviors of the integrated intensities corresponding to the volume fractions of β′ and β″ precipitates. For example, the SAXS profiles in the β″ regime, $0.04 \leqslant Q \leqslant 0.1\ \text{Å}^{-1}$, show decreasing integrated intensities as the aging time increases, implying the dissolution of the β″ precipitates. In contrast, the concurrent β′ precipitates still shows a typical precipitation behavior from the time evolution of the integrated intensities in the β′ regime. Obviously, the concurrent phase transformations of β″ and β′ precipitates entered the different stages.

Furthermore, Fig. 3(c) shows the selected SAXS profiles collected during a long aging time ranging from 210 to

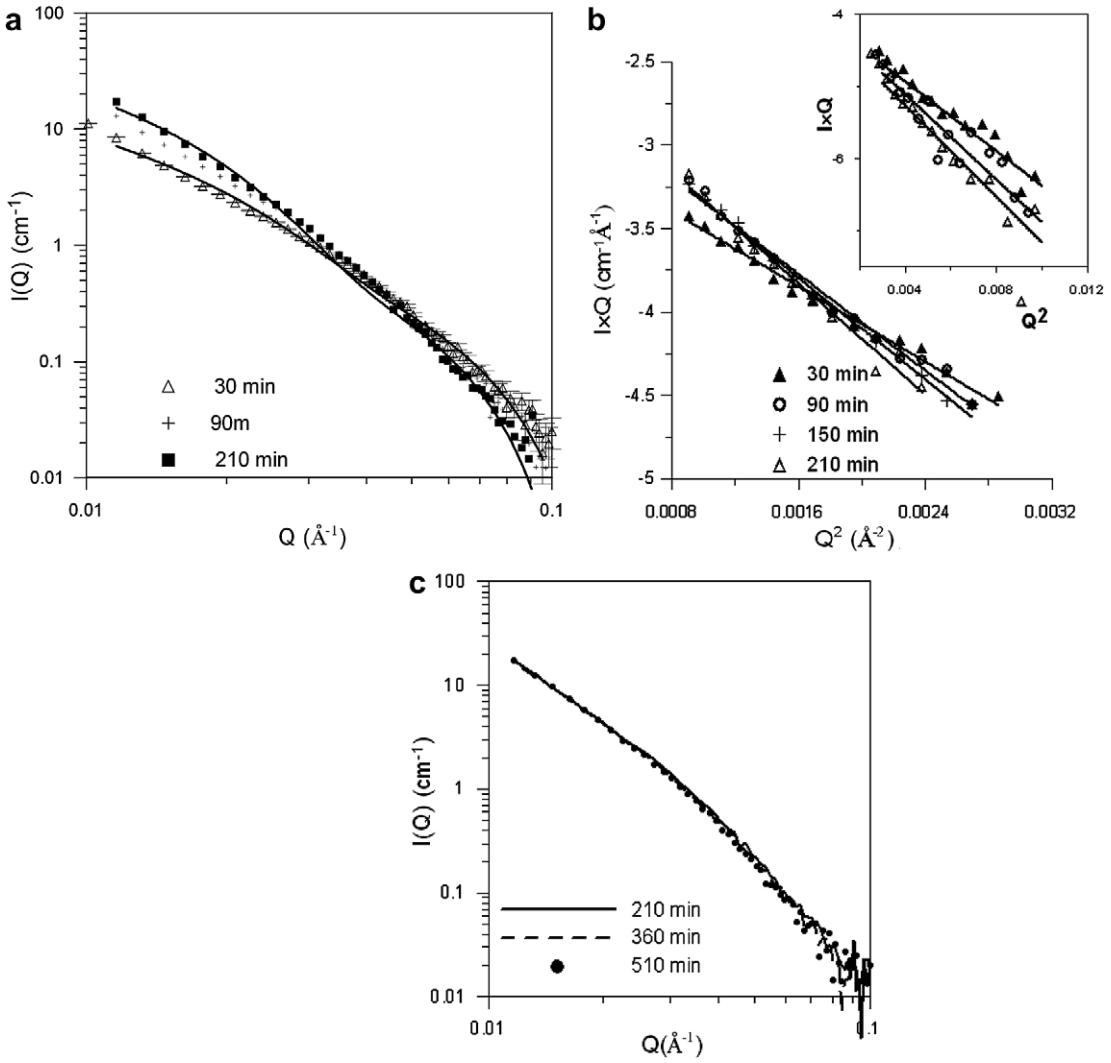

Fig. 3. (a) Selected time-dependent and cluster-subtracted SAXS profiles (double-log scale) that show the structural evolution of precipitates in the AA 6022 alloy aged at 260 °C for 210 min. The SAXS profiles are fitted (solid lines) using the model of Eq. (3). (b) The selected SAXS profiles are fitted (solid lines) in the low-Q region and the intermediate- to high-Q region (inset), respectively, using the Kratky–Porod approximation (linear plot) for the temporal evolutions of the radii of the β′ and β″ precipitates. (c) The cluster-subtracted SAXS profiles (double-log scale) selected for the temporal evolution of precipitates during a long aging period at 260 °C.

720 min. The temporal evolution of the SAXS profiles in the β′ regime shows a time-independent behavior, while that of the SAXS profiles in the β″ regime shows only a slight reduction of the integrated intensities. The corresponding structural parameters, the best-fit values of radii and relative volume fraction of β′ and β″ precipitates by the use of model fitting of Eq. (3) are listed in Table 2. The TEM observation for this SAXS specimen aged at 260 °C (Fig. 4) shows that the needle-like β″ precipitates coexist with the rod-like β′ precipitates with a similar length ($\geqslant$200 nm). Both can be easily identified due to the large difference in radius. The observed TEM result is, in general, close to the SAXS analysis result (~3 nm for β″ precipitate radius and ~10 nm for β′ precipitates radius). We summarize the time-dependent radii and relative volume fractions of the β″ and β′ precipitates during the whole isothermal aging process at 260 °C in Figs. 5(a) and (b). A TEM result [18] is also shown in Fig. 5(b) for comparison. (Note that all types of β′ precipitates, including β′, β'_A and β'_B, are treated as the same precipitates in this study.)

Precipitation involves three major coupled processes: nucleation, growth and coarsening. The first two processes are driven by the free energy change of a system during phase separation, and will be completed when the equilibrium volume fraction of precipitates is reached. In contrast, the coarsening stage (or Ostwald ripening) is driven only by a reduction of interface energy, and is usually considered as the last stage of precipitation, featured with a fixed equilibrium volume fraction of precipitates. According to the numerical simulation [30,31] of classic theory, when the system enters a coarsening stage, the growth of the volume fraction of precipitates will saturate asymptotically. The growth rate of precipitates decreases gradually from a power law behavior $\propto t^{1/2}$ (typical growth regime) to $\propto t^{1/6}$

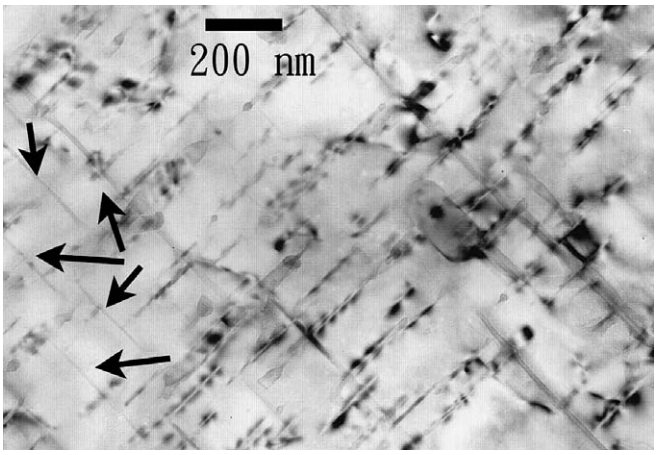

Fig. 4. Bright-field TEM micrograph of AA 6022 alloy aged at 260 °C for 720 min. The widths of needle-like (indicated by the arrows in the lower left part) and rod-like morphologies represent the diameters of the β″ and β′ precipitates oriented along $\langle 0\,1\,0\rangle_{Al}$ directions.

when entering the early stage of the coarsening regime (or transition regime) [27]. The transition behavior approaches asymptotically a saturation state [28,31]. Nevertheless, in the late stage of the coarsening regime (LSW coarsening [27]), the growth rate speeds up again with a power law behavior of $\propto t^{1/3}$. From the beginning of the isothermal aging shown in Fig. 5, the rapidly growing radius and volume fraction of β′ precipitates with aging time still exhibit typical nucleation and growth behavior. After $t = 210$ min, the radius and volume fraction evolutions of β′ precipitates with aging time change to typical behavior of early-stage coarsening. It can be deduced that this coarsening stage of β′ precipitates is developed mainly by the length growth. The volume fraction of the β″ precipitates remains in the nucleation and growth step during continuous heating, and reaches a peak value 30 min after isothermal aging at 260 °C. Thereafter, the volume fraction of β″ precipitates starts to decrease significantly with the aging time, and at $t = 510$ min, saturates at a value of 65% of the maximum volume fraction.

Our SAXS results reveal that 35% of the β″ phase can be consumed by dissolution and/or transformation (β″ → β′ precipitates) within 8 h of isothermal aging, and then remain at a constant volume fraction. In contrast, the TEM result [18] in Fig. 5(b) shows that the β″ phase decays rapidly and vanishes totally to zero. The SAXS results also show the slight growing radius of β″ precipitates with aging time during 30–210 min. Compared to the constant radius during continuous heating, the growing radius might illustrate a feature of the coarsening regime. The saturation of growing radius at $t = 210$ min can be explained by the fact that the size increase in the coarsening regime is continued by the length increase of β″ precipitates with an inert radius.

An interesting issue is how the β″ phase transforms into the β′ phase. A previous TEM study [16] proposed that the β″ phase could transform into the metastable β'_A and β'_B phases from the viewpoint of the atomic composition of precipitates. Our in situ SAXS study (see Fig. 5(b)) demonstrates the rapid nucleation and growth of β′ phase is concurrent with the significant dissolution of β″ phase during $t = 30$–210 min. In principle, the sites of dissolved β″ precipitates are also more favored as the nucleation sites of β′ precipitates. We do not support the proposition that the metastable phases of β′ series are transformed directly from the β″ phase because the growth and formation of the β″ and β′ precipitates are characterized by the independent nucleation, growth and coarsening processes.

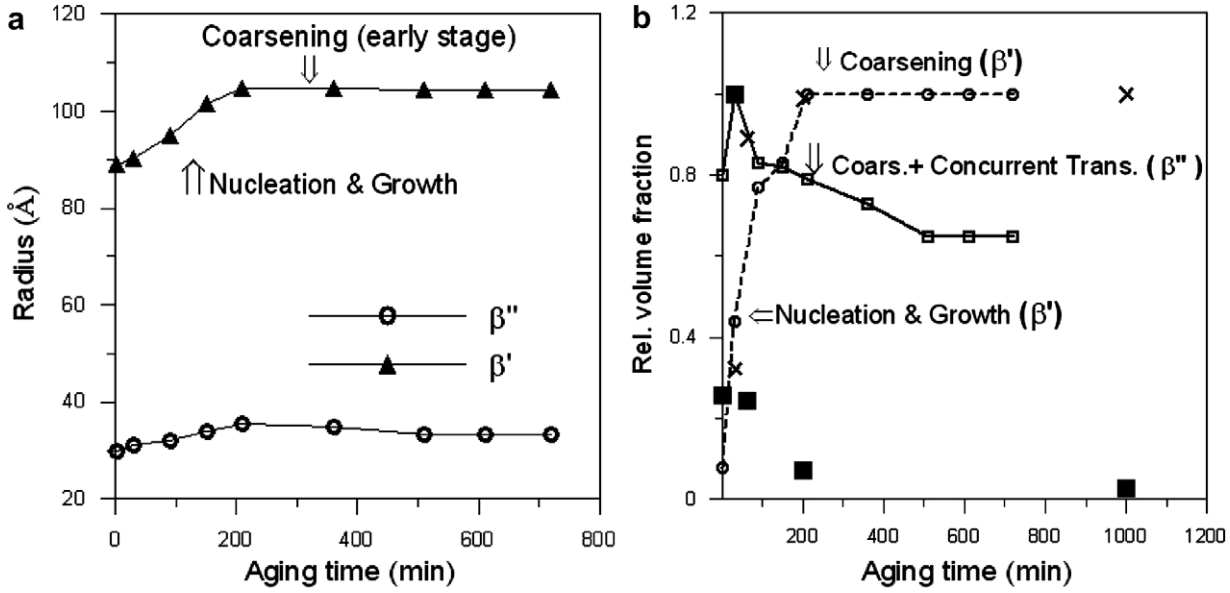

Fig. 5. (a) Temporal evolutions of the radii of the β″ and β′ precipitates extracted by the model fitting of the SAXS data of the AA 6022 alloy aged at 260 °C. (b) Comparison of the temporal evolutions of relative volume fractions of the precipitates obtained by the same SAXS analysis (β″ phase: open square; β′ phase: open circle) and TEM result [18] (β″ phase: filled square; β′ phase: cross).

The limitation determining particle size depends mainly on the Q range of a measured scattering profile. As a rule of thumb of $QR \leqslant 1.0$, we measured the scattering profile in the Q range covering $Q = 1/R$ for determining particles with a radius R. The Q range used in this study, 0.01–0.1 Å^{-1}, corresponds to an observable size scale from the order of 10 nm to the order of 1 nm for spherical clusters or needles. According to this principle, the Q range covered by the SAXS data (0.01–0.1 Å^{-1}) in this study cannot resolve unequivocally sizes larger than ~31 nm ($\pi/Q_{\min}$), according to the model-independent Kratky–Porod approximation. Nevertheless, with model-dependent fitting, we may extrapolate a length scale of 150–1 nm or less, with a larger uncertainty in the fitted length.

With rigorous SAXS analysis, one can determine the absolute volume fraction of nanoparticles in bulk materials, including alloy precipitates, as already demonstrated in many SAXS applications [20–23]. Unfortunately, because of interference by the preexisting natural clusters and the complex crystal structures in our case, we have difficulty in correlating the relative to the absolute volume fraction of the precipitates.

3.3. Comparison of precipitation behaviors of β″ phases in different Al–Mg–Si alloys aged at 180 °C

The in situ SAXS and TEM results presented here yield the temporal evolution of the nanoprecipitate structure in AA 6111 alloy aged at 180 °C (only β″ precipitation occurs at this temperature), in terms of radius, length and volume fraction. The SAXS analytical method and results for AA 6022 alloy aged at 180 °C are reported in detail elsewhere [25]. This section compares the precipitation kinetics and behavior of β″ precipitates in AA 6111 and AA 6022 alloys, taking into account the effects of Mg and Si contents.

Fig. 6(a) presents selectively the time-dependent SAXS profiles obtained from both Al–Mg–Si alloys during heating from RT to 180 °C and during subsequent artificial aging at 180 °C. The standard deviation of the SAXS profiles presented in Fig. 6(a) is within ±2% except for that of AA 6022 at RT. As mentioned previously, the power law scattering of Q^{-4} in the low-Q region corresponds to the asymptotic scattering behavior of other large particles. The SAXS profiles in the intermediate-Q region measured at RT and during isothermal aging at 180 °C are attributed to scatterings from the natural aging clusters and β″ precipitates, respectively. According to Fig. 6(a), the SAXS intensity in the intermediate-Q region of the AA 6111 alloy at RT considerably exceeds that of the AA 6022 alloy, demonstrating that AA 6111 has more natural aging clusters formed at RT. Our rough comparison of TEM observations between AA 6022 and AA 6111 alloy samples naturally aged at RT (not shown here) also confirms this SAXS measurement. Because the composition of the natural aging cluster is similar to that of the β″ precipitate (Mg/Si ratio is 1) [2,9], AA 6111 alloy with a higher MgSi content produces more clusters. The SAXS profiles measured during the heating process and the SAXS profile of the alloy isothermally aged at 180 °C for 60 min (not shown here) are nearly the same, indicating that the incubation period is ~60 min (during which no structural change occurs). The incubation period of AA 6111 alloy exceeds that, ~30 min, of the AA 6022 alloy [25], because the effect of more natural aging clusters greatly reduces the quench-in vacancies at RT, and thus the diffusion rate of solute atoms. The similar incubation behavior in the pre-aged Al–Mg–Si alloys was also validated independently by a recent thermal analysis [33].

After 60 min of aging, the intensity of the SAXS profiles in Fig. 6(a) increases with the aging time in the intermediate-Q region ($Q \geqslant 0.03$ Å^{-1}), indicating increases in the size and volume fraction of β″ precipitates. The coexistence of hard-dissolved natural aging clusters and precipitates during precipitation from the SAXS profiles measured during isothermal aging at 180 °C can be expressed as

$$I(Q) = I_{\text{precip}}(Q) + \alpha \cdot I_{\text{cluster}}(Q, t_0) + B \tag{4}$$

where the time-dependent $I_{\text{precip}}(Q)$ is the scattering contribution of the precipitates. α is the percentage of the surviving or non-dissolved clusters during artificial aging. $I_{\text{cluster}}(Q, t_0)$ represents the SAXS profile measured at RT corresponding to the scattering contribution of all initial clusters. B is a constant incoherent background. The SAXS intensity of the precipitates of the artificially aged alloy is modeled as

$$I_{\text{precip}}(Q) = AQ^{-4} + \eta(\Delta\rho)^2 V_{\text{P}} \tilde{P}(Q) \tag{5}$$

where the first term refers mainly to the lowest-Q region, with A being a constant, describing the sharp boundary effect of large particles. The second term is the cylindrical form factor that relates to scattering from the β″ precipitates.

The SAXS background profile, $I_{\text{cluster}}(Q, t_0)$ in Eq. (4), can be regarded as a sum of $C \cdot Q^{-4}$ (C is a constant) for the large particles and the intensity scattered from the small natural aging clusters (GP zones). Note that $I_{\text{precip}}(Q)$ and $I_{\text{cluster}}(Q, t_0)$ include the Q^{-4} power law scattering terms. The volume fraction of large particles can be assumed not to change throughout natural aging or artificial aging, so the relationship $A + \alpha \cdot C = C$ can be deduced by substituting Eq. (5) into Eq. (4). This relationship constraints the effect of large particles and is maintained during the model fitting using Eqs. (4) and (5). With the measured $I_{\text{cluster}}(Q, t_0)$, the structural parameters $\eta(\Delta\rho)^2$, R, L, α, A and C are thus extracted by the model fitting, as summarized in Table 3. The SAXS profiles from which the cluster contribution is subtracted using $\alpha \cdot I_{\text{cluster}}(Q, t_0)$, i.e., $I_{\text{precip}}(Q)$, are fitted well using Eq. (5) (Fig. 6(b) displays the selected fitting curves). The model-fitted radii, indicating time-independent behavior, are consistent with those obtained by the model-independent method (Kratky–Porod approximation) and the TEM observation shown in Figs. 6(c) and 7, respectively. The mean radius of β″ precipitates, 1.78 nm, determined by model fitting for

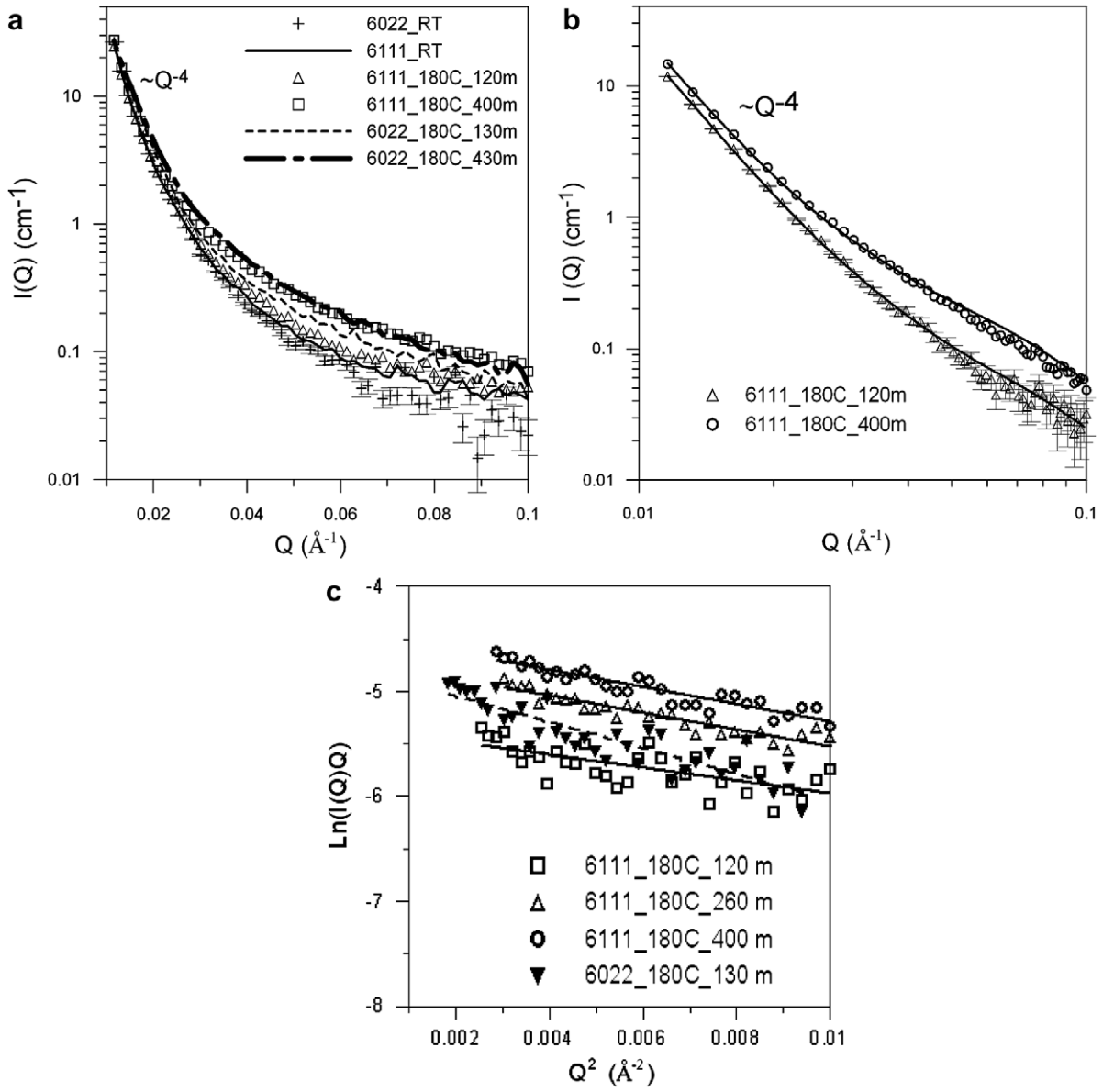

Fig. 6. (a) Selected time-dependent SAXS profiles (log-to-linear plot) of the naturally aged AA 6022 and AA 6111 alloys during heating and subsequent isothermal artificial aging at 180 °C, revealing the structural evolution of precipitates with aging time. (b) Cluster-subtracted SAXS profiles (double-log plot) with a best-fit α of 0.5. Calculated SAXS profiles (solid lines) simulate well the measured SAXS data, $I_{\text{precip}}(Q)$. (c) The selected SAXS profiles of the AA6111 alloy are fitted (solid lines) using the Kratky–Porod approximation for the temporal evolution of the radius of the precipitates. The SAXS profile of AA 6022 alloy is fitted (dash line), indicating a larger radius (slope of fitted line).

the AA 6111 alloy is smaller than that for the AA 6022 alloy, 2.77 nm. This difference between the radii is also demonstrated by comparing the slopes of the lines fitted using Kratky–Porod approximations with the SAXS data obtained for both alloys (Fig. 6(c)). The smaller radius for the AA 6111 alloy can be attributed to the reduced solute atoms due to more natural aging clusters formed. The model-fitted lengths for the AA 6111 alloy are similar to those for the AA 6022 alloy.

For the isothermal aging of naturally aged alloys, the DSC result shows only characteristics of the β″ precipitation during 180 °C aging, and there is no sign of GP peak [1]. In the current study, the GP zones are the natural aging clusters serving as the β″ nucleation sites. In principle, it will be increasingly difficult to separate the SAXS contributions from two coexistent phases (for instance, GP-zones and β″ phase) in a system using the method developed in this study, when the characteristic sizes of the two phases become increasingly close.

The existence of Cu in the clusters can increase in principle the scattering contrast between the precipitates and the Al matrix, and thus enhance the SAXS intensity observed for the AA 6111 alloy, compared to that for the AA 6022 alloy. In the current study, we could not evaluate quantitatively the scattering contrast effect due to the Cu content. Therefore, we use the SAXS intensity at RT as a part background subtraction and adopt separately a relative volume fraction expression in the data analysis.

Table 3
Radii, lengths and relative volume fractions of β″ precipitates determined by the model fitting of SAXS data of the AA6111 alloy during isothermal aging at 180 °C

Aging time (min)	R (nm)	L (nm)	Relative volume fraction[a]
120	1.65 ± 9%	14.7 ± 9%	0.43 ± 15%
260	1.90 ± 3%	14.9 ± 4%	0.74 ± 5%
340	1.77 ± 3%	15.8 ± 4%	0.87 ± 6%
400	1.80 ± 2%	16.2 ± 4%	1.00 ± 5%

The absolute and relative volume fractions (β″ + Q') obtained from the TEM study [6] for the naturally aged AA 611 alloy aged at 180 °C: (1) $f_{Abs} = 2.6 \times 10^{-3}$, $f_{Rel} = 33\%$ for 60 min aging; (2) $f_{Abs} = 7.9 \times 10^{-3}$, $f_{Rel} = 100\%$ for 420 min aging.

[a] The parameter determined by the fitted $\eta(\Delta\rho)^2$ value normalized to its maximum.

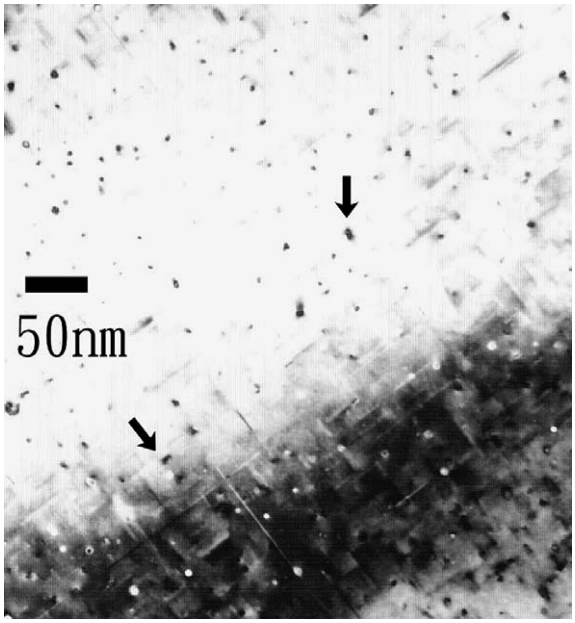

Fig. 7. Bright-field TEM micrograph ($[100]_{Al}$ zone axis) of AA 6111 alloy aged at 180 °C for 400 min. Most dots display the circular cross-section of needle-like β″ precipitates. Few dots (as indicated by the arrows) show the lath-like cross-section of Q' phase, which is similar to other TEM observations [5,6].

However, the SAXS profiles of AA 6111 alloy aged for 400 min match closely those of AA 6022 alloy aged for 430 min, as shown in Fig. 6(a). This result indicates that in this aging range, effect of Cu-containing precipitates (Q' or β″ phases) in AA 6111 alloy does not obviously influence the scattering contrast of the precipitates.

Because the AA 6111 alloy is an Al–Mg–Si alloy containing Cu, another type of precipitate with a higher Cu content, called Q' phase, coexists with the β″ precipitates during aging at 180 °C. The previous TEM studies [5,6] showed that Q' phase is lath-like (or plate-shaped) and is similar in cross-section to β″ phase. Accordingly, the main effect of Q' phase on the SAXS profiles is to change the scattering contrast. A typical TEM observation [5] of the AA 6111 alloy aged at 180 °C for 11 h shows the needle-like β″ phase of 3.0 × 3.0 nm in cross-section and 20 nm long, and the lath-like Q' phase of ~2.0 × 5.0 nm in cross-section and ~100 nm in length. Fig. 7 shows our TEM observation of the β″ phase and the coexisting Q' phase, which is consistent in morphology with the TEM result discussed above. Previous work [6] pointed out that within ~7 h of aging at 180 °C, the volume fraction of β″ precipitates is 2–4 times that of the Q' phase. In contrast, the Q' phase is the major phase for the AA 6111 alloy aged at $T \geqslant 250$ °C or over-aged at 180 °C. Our TEM observation (Fig. 7) also confirms that β″ phase is the dominant one and few Q' precipitates coexist (shown by the arrows). Additionally, the SAXS profiles agree with the prediction for the length of β″ needles, indicating the amount of Q' phase is small.

Based on the characteristics of similar cross-section, the present study considers the minor Q' phase to be in the same category as the β″ phase. Thus, the β″ radius determined from the SAXS profile involves the error source resulting from the Q' phase. The error source is tolerable in the present aging condition. For the AA 6111 alloys aged at $T \geqslant 250$ °C or over-aged at 180 °C, the error source becomes significant due to the larger size and predominance of Q' phase.

The scattering contrasts from the β″ precipitates with and without Cu, the Q' phase and the Q' precursor construct a convoluted contrast based on similar SAXS profiles. Thus, the error source of the relative volume fraction determined comes from the variation in the scattering contrast weighted by various precipitates. The contrast values $\Delta\rho$ obtained from the SAXS data fitting of AA 6111 alloy remain quite stable during aging at 180 °C. Therefore, it can be concluded that precipitates' evolution during aging does not influence the convoluted contrast.

Fig. 8 compares the temporal evolutions of the relative volume fractions of precipitates in both AA 6022 and AA 6111 alloys obtained by SAXS model fitting with that for an Al–0.63% Mg–Si alloy obtained by the numerical

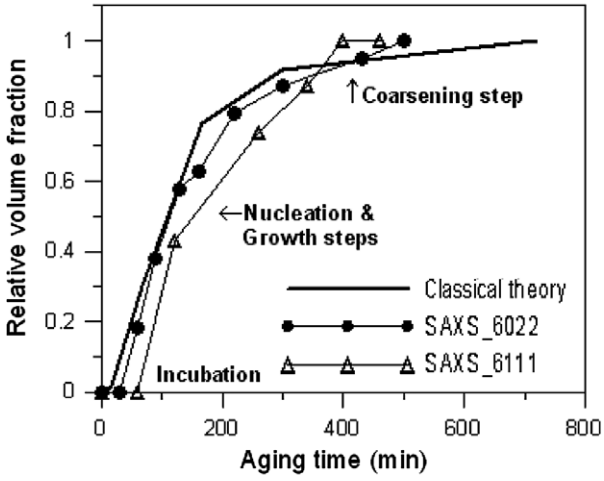

Fig. 8. Comparison of temporal evolutions of the relative volume fractions of precipitates determined from the SAXS model-fitting results for both alloys aged at 180 °C with that predicted by numerical simulation [28] based on classic theory [27].

simulation [28] based on the classic model. The numerical simulation was based on artificial aging at 180 °C without natural aging treatment. All temporal evolutions presented in Fig. 8 are characterized effectively by coupled nucleation, growth and coarsening. The SAXS results for both alloys clearly indicate the incubation period associated with the natural aging effect. The incubation period of AA 6111 alloy, ~60 min, exceeds that of AA 6022 alloy, ~30 min, because the former alloy has a higher MgSi content. However, the incubation period does not influence the time required for the relative volume fraction to reach one.

4. Conclusions

With the high-flux SAXS results together with the new SAXS analysis approach, we have established an algorithm to extract the structural evolution of metastable β″ and β′ phases of Al–Mg–Si alloys. Justified by the consistent TEM result, this methodology is of potential applicability in a wider context of multi-component age-hardening alloys. The in situ SAXS, TEM and numerical simulation based on the classic theory together can provide an integrated understanding of the transformation kinetics of the precipitates. We summarize the precipitation kinetics and concurrent transformation behaviors of the metastable phases observed as follows:

1. For the naturally aged AA 6022 alloy, the β″ and β′ phases begin to form at 211 and 235 °C, respectively, during continuous heating. The volume fraction evolutions of β″ and β′ precipitates with aging time during continuous heating and subsequent isothermal aging at 260 °C can be well characterized by the typical nucleation, growth and coarsening stages. The β″ and β′ precipitates reach the coarsening stages at $t = 30$ and 210 min, respectively. Afterwards, the β″ precipitates start to dissolved partially and/or transformed partially to β′ phase, then saturate with a volume fraction of 65% of the maximum value after $t = 510$ min.
2. The radius of rod-like β′ precipitates increases obviously from 9.1 ± 0.1 nm to 10.5 ± 0.2 nm during the nucleation and growth stage, and then remains approximately constant during the coarsening stage ($210 < t < 720$ min) where the length starts to grow significantly. In contrast, the needle-like β″ precipitates retain a constant radius of ~3.1 nm but undergo a rapid length growth from 18.3 nm to a length much larger than 100 nm during nucleation and growth stages. In the coarsening stage, the radius of β″ precipitates grows slightly from 3.1 ± 0.06 nm to 3.4 ± 0.07 nm during 30–210 min, then followed by an increase mainly in the length. The slight radius increase might be related to some β″ precipitates serving as β′ nucleation sites.
3. For the AA 6111 alloy aged at 180 °C up to 400 min, with the main precipitates of β″ phase, the structural evolution of the precipitates also exhibits a constant radius of ~1.8 nm and an increase in length with aging time. The longer incubation period in the early stage of precipitation, compared to the AA 6022 alloy, is attributed to more natural clusters. No clear effect of Cu can be identified in the structural evolution of the precipitates.

References

[1] Miao WF, Laughlin DE. Scripta Mater 1999;40:873.
[2] Edwards GA, Stiller K, Dunlop GL, Couper MJ. Acta Mater 1998;46:3893.
[3] Marioara CD, Andersen SJ, Jansen J, Zandbergen HW. Acta Mater 2001;49:321.
[4] Marioara CD, Andersen SJ, Jansen J, Zandbergen HW. Acta Mater 2003;51:789.
[5] Perovic A, Perovic DD, Weatherly GC, Lloyd DJ. Scripta Mater 1999;41:703.
[6] Esmaeili S, Wang X, Lloyd DJ, Poole WJ. Metall Trans A 2003;34:751.
[7] Donnadieu P, Carsughi F, Redjaïmia A, Diot C, Lapasset GJ. Appl Crystallogr 1998;31:212.
[8] Maruyama N, Uemori R, Hashimoto N, Saga M, Kikuchi M. Scripta Mater 1997;36:89.
[9] Maruyama N, Hono K. Acta Mater 1999;47:1537.
[10] Esmaeili S, Lloyd DJ, Poole WJ. Acta Mater 2003;51:3467.
[11] Bryant JD. Metall Trans A 1999;30:8.
[12] Gupta AK, Lloyd DJ, Court SA. Mater Sci Eng A 2001;301:140.
[13] Dumolt SD, Laughlin DE, Williams JC. Scripta Metall 1984;18:1347.
[14] Matsuda K, Tada S, Ikeno S, Sato T, Kamio A. Scripta Metall Mater 1995;32:1175.
[15] Matsuda K, Sakaguchi Y, Miyata Y, Uetani Y, Sato T, Kamio A, et al. J Mater Sci 2000;35:179.
[16] Matsuda K, Ikeno S, Sato T. Science, technology and education of microscopy: an overview. Formatex Microscopy Book Series, 2002. p. 152.
[17] Matsuda K, Ikeno S, Matsui H, Sato T, Terayama K, Uetani Y. Metall Trans A 2005;36:2007.
[18] Matsuda K, Uetani Y, Sato T, Ikeno S. Metall Trans A 2001;32:1293.
[19] Massardier V, Epicier T, Merle P. Acta Mater 2000;48:2911.
[20] Guinier A, Fournet G. Small angle X-ray scattering. New York (NY): Wiley; 1955.
[21] Glatter O, Kratky O. Small angle X-ray scattering. New York (NY): Academic Press; 1982.
[22] Tsao CS, Chang HL, Jeng US, Lin JM, Lin TL. Polymer 2005;46:8430.
[23] Tsao CS, Chen CY, Huang JY. Phys Rev B 2004;70:174104.
[24] Schiffmann R, Haug J, Banhart J. Proceedings of the 9th International Conference on Aluminum Alloys, Institute of Materials Engineering Australasia Ltd, 2004. p. 604.
[25] Tsao CS, Jeng US, Chen CY, Kuo TY. Scripta Mater 2005;53:1241.
[26] Poole WJ, Lloyd DJ, Embury JD. Mater Sci Eng A 1997;234–236:306.
[27] Wagner R, Kampmann R. Materials science and technology: a comprehensive treatment, vol. 5. Weinheim: VCH; 1991. p. 213.
[28] Myhr OR, Grong Ø. Acta Mater 2000;48:1605.
[29] Myhr OR, Grong Ø, Andersen SJ. Acta Mater 2001;49:65.
[30] Deschamps A, Bréchet Y. Acta Mater 1999;47:293.
[31] Werenskiold JC, Deschamps A, Bréchet Y. Mater Sci Eng A 2000;293:267.
[32] Glasstone S, Sesonske A. Nuclear reactor engineering. New York (NY): Van Nostrand Reinhold; 1981 [Chapter 7].
[33] Esmaeili S, Lloyd DJ. Acta Mater 2005;53:5257.